Electronic Supplementary Information

Cyano-Bridged Coordination Polymer Hydrogel-Derived Sn–Fe Binary Oxide Nanohybrids with Structural Diversity: From 3D, 2D, to 2D/1D and Enhanced Lithium-Storage Performance

Weiyu Zhang,[a] Xiaoshu Zhu,[a] Xuguang Chen,[a] Yiming Zhou,[a] Yawen Tang,[a] Liangxin Ding*[b] and Ping Wu*[a]

[a]Jiangsu Key Laboratory of New Power Batteries, Jiangsu Collaborative Innovation Center of Biomedical Functional Materials, School of Chemistry and Materials Science, Nanjing Normal University, Nanjing 210023, China.

[b]School of Materials Science and Engineering, Key Laboratory of Advanced Energy Storage Materials of Guangdong Province, South China University of Technology, Guangzhou 510640, China.

*E-mail: lxding@scut.edu.cn (L.D.); zjuwuping@njnu.edu.cn (P.W.).

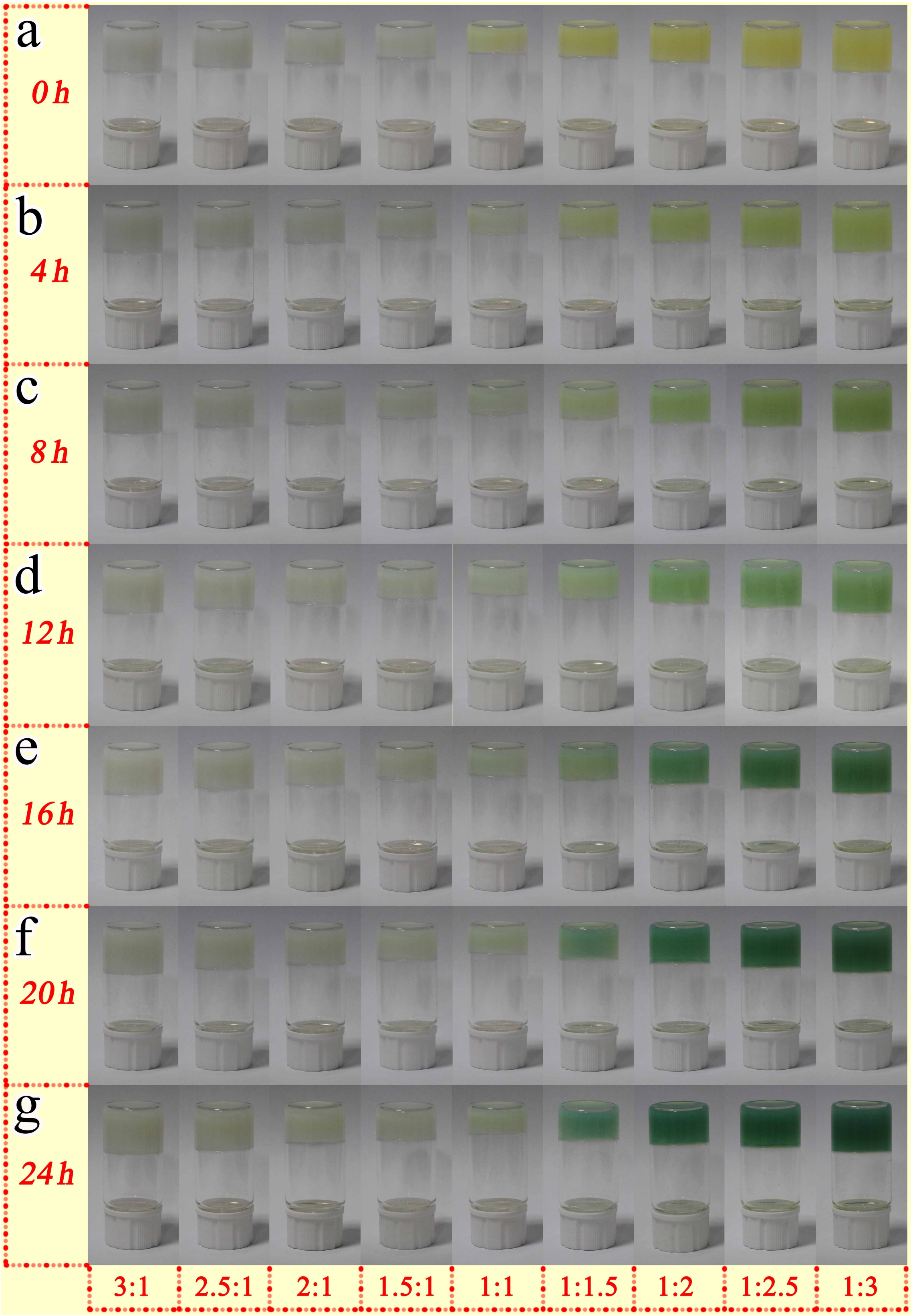

Fig. S1 Photographs of the Sn–Fe cyanogels with different molar ratios of Sn/Fe from 3:1 to 1:3 taken by every four hours within the initial 24 h: (a) 0 h, (b) 4 h, (c) 8 h, (d) 12 h, (e) 16 h, (f) 20 h, and (g) 24 h.

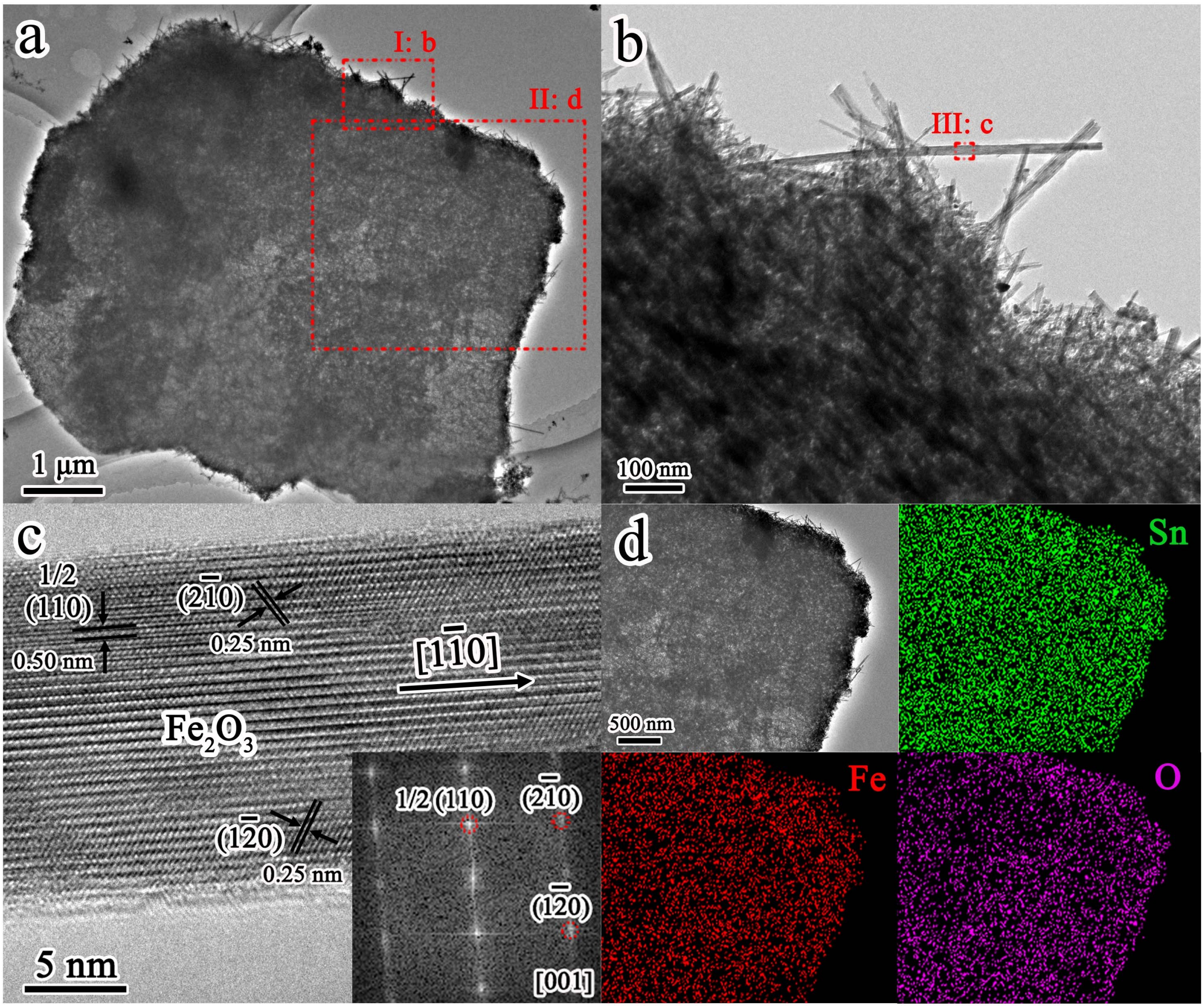

Fig. S2 Morphological and structural features of the 2D/1D SnO_2–Fe_2O_3 hierarchitectures: (a, b) TEM images, (c) HRTEM image and its FFT pattern (inset), and (d) TEM-EDS elemental mappings of Sn (green), Fe (red), and O (purple).

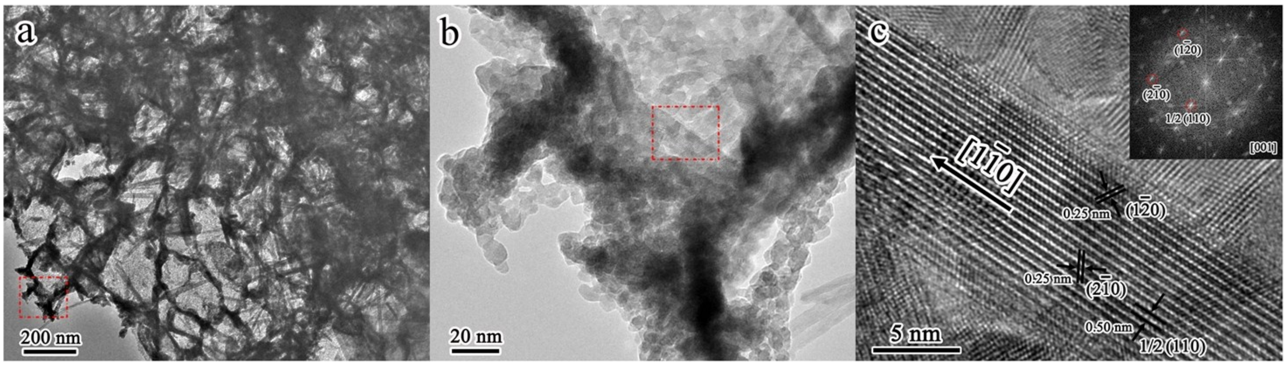

Fig. S3 Morphological and structural features of the 2D/1D SnO_2–Fe_2O_3 hierarchitectures: (a, b) TEM images and (c) HRTEM image and its FFT pattern (inset).

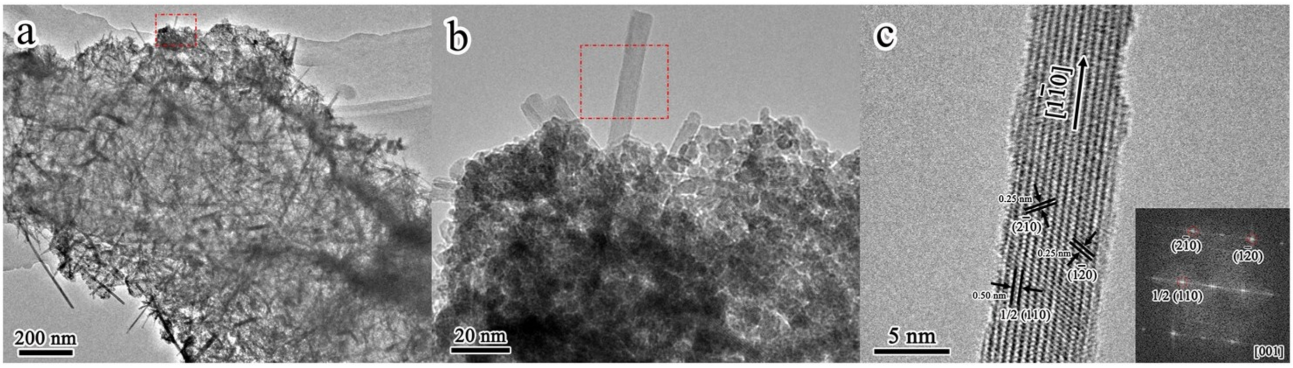

Fig. S4 Morphological and structural features of the 2D/1D SnO_2–Fe_2O_3 hierarchitectures: (a, b) TEM images and (c) HRTEM image and its FFT pattern (inset).

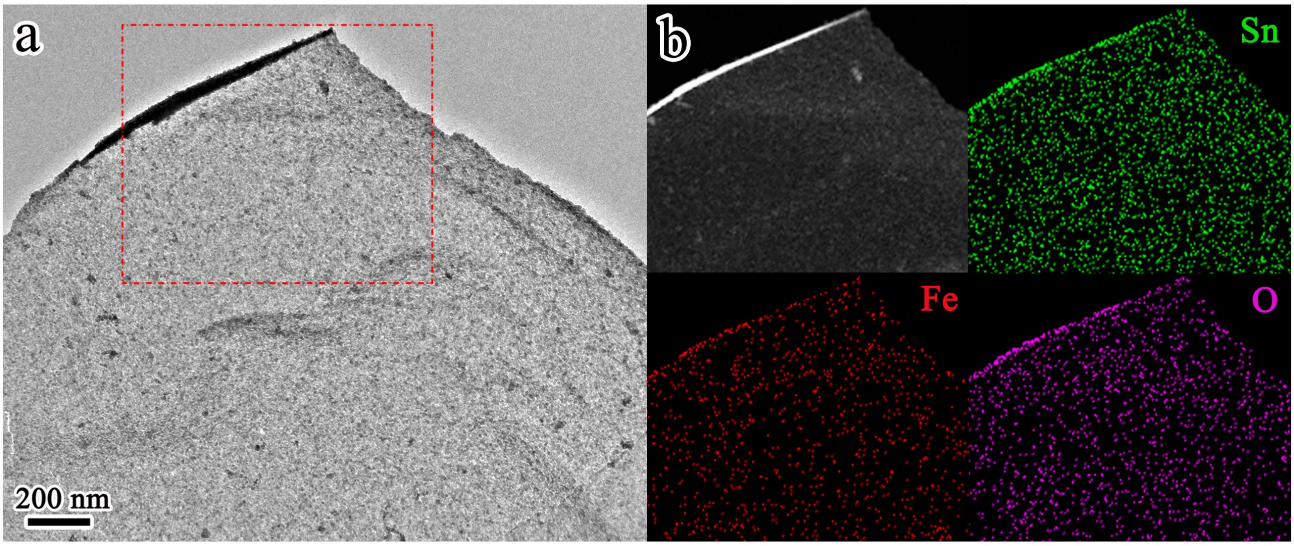

Fig. S5 TEM-EDS elemental mappings of the 2D SnO_2–Fe_2O_3 nanosheets.

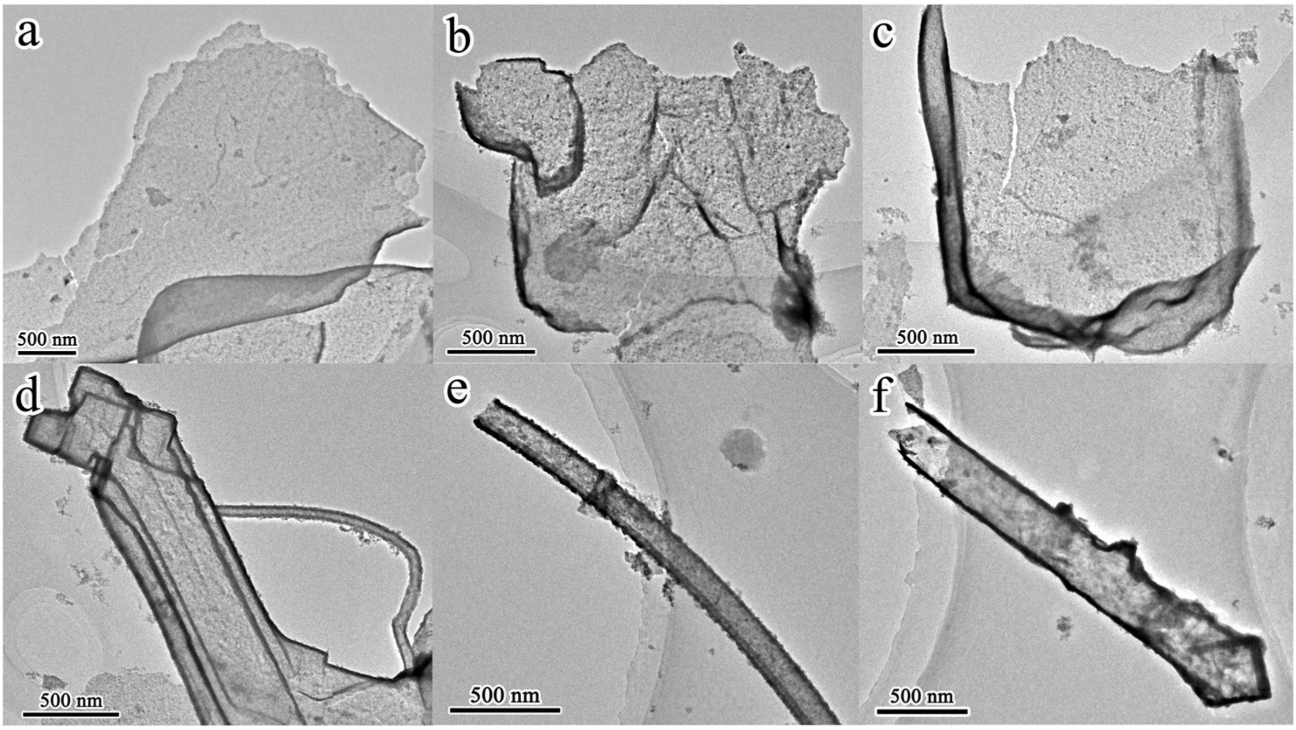

Fig. S6 TEM images of the semi-folded (a), crumpled (b), and scrolled (c-f) 2D SnO_2–Fe_2O_3 nanosheets.

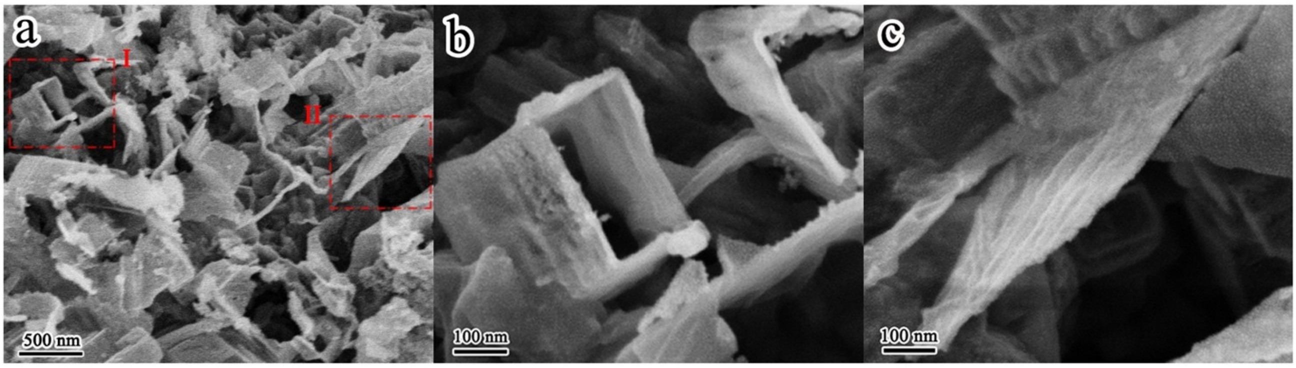

Fig. S7 SEM images of the 2D SnO_2–Fe_2O_3 nanosheets.

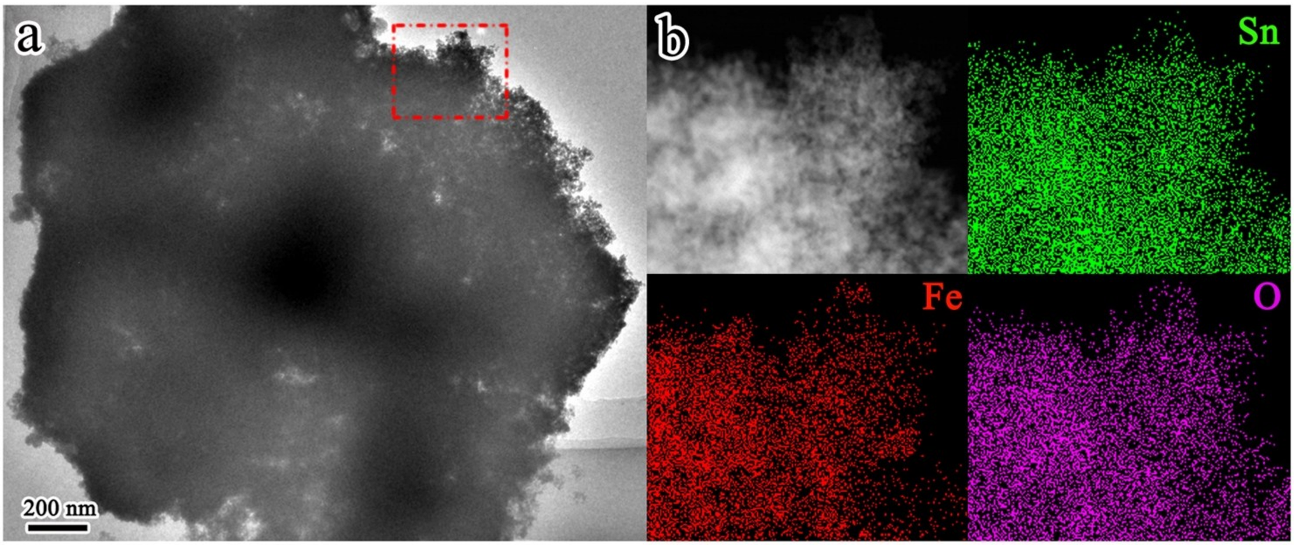

Fig. S8 TEM-EDS elemental mappings of the 3D SnO_2–Fe_2O_3 networks.

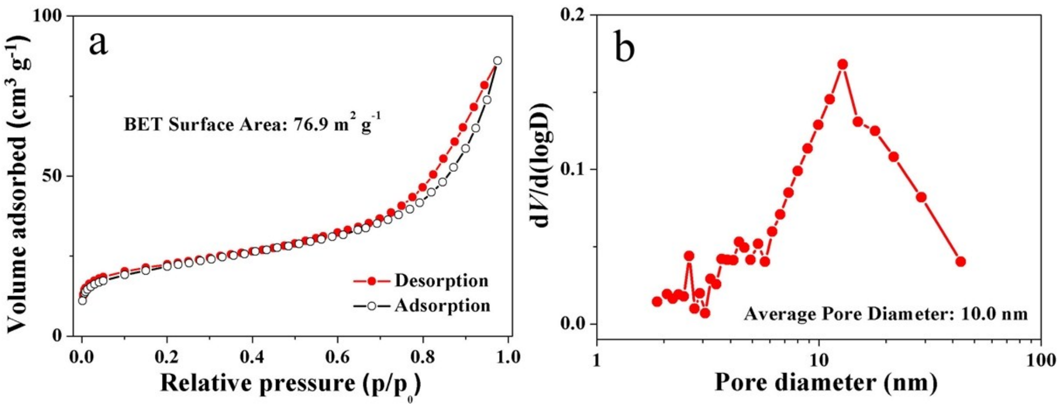

Fig. S9 Nitrogen adsorption/desorption isotherms (a) and pore diameter distribution from the desorption branch (b) of the 2D/1D SnO_2–Fe_2O_3 hierarchitectures.

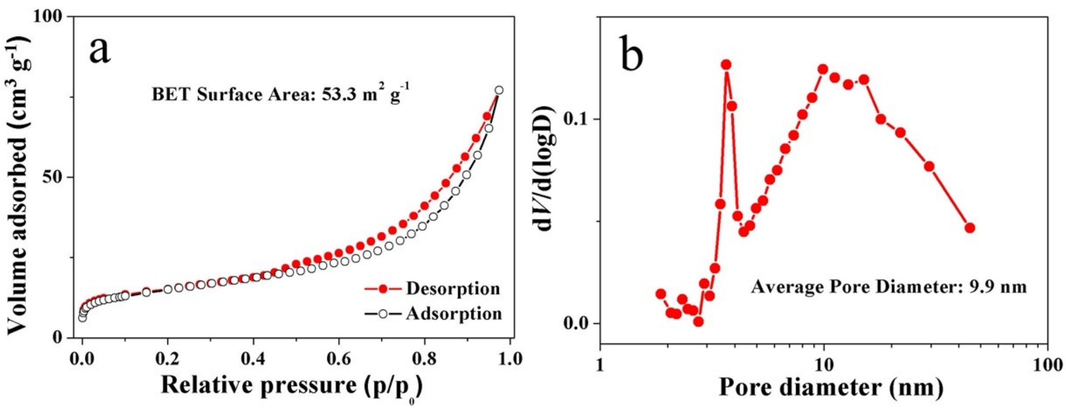

Fig. S10 Nitrogen adsorption/desorption isotherms (a) and pore diameter distribution from the desorption branch (b) of the 2D SnO_2–Fe_2O_3 nanosheets.

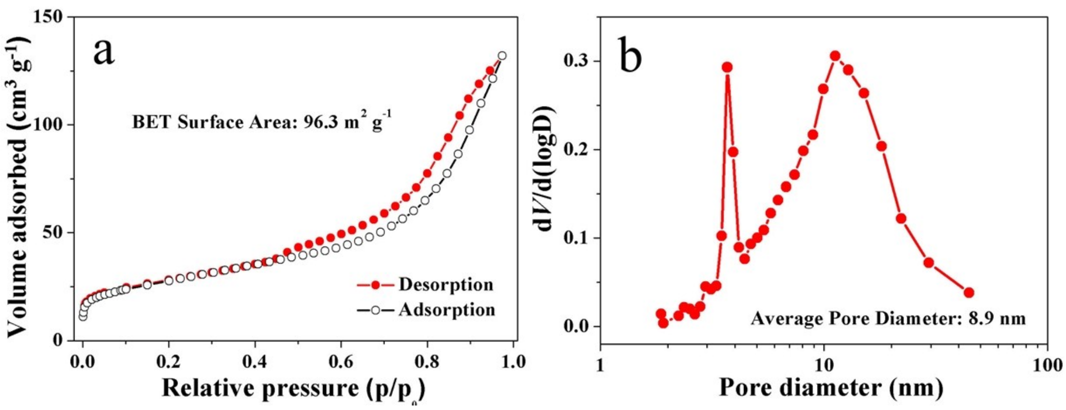

Fig. S11 Nitrogen adsorption/desorption isotherms (a) and pore diameter distribution from the desorption branch (b) of the 3D SnO_2–Fe_2O_3 networks.

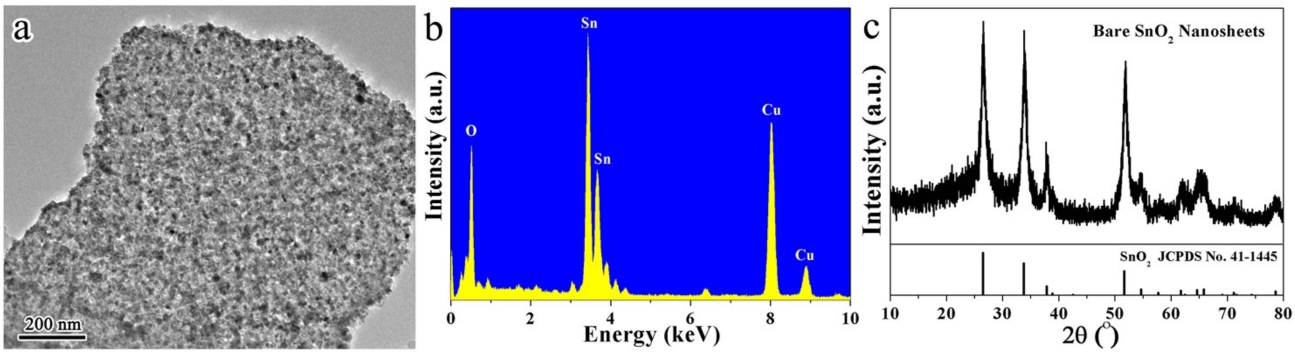

Fig. S12 Morphological, compositional, and structural features of the bare SnO_2 nanosheets: (a) TEM image, (b) EDS spectrum, and (c) XRD pattern.

Bare SnO_2 nanosheets has been obtained by dissolving Fe_2O_3 component in 2D SnO_2–Fe_2O_3 nanosheets with a 6 M HCl solution (Fig. S12). As seen from the TEM image, the product retains the 2D sheet-like morphology of the 2D SnO_2–Fe_2O_3 nanosheets after the dissolution of Fe_2O_3 component (Fig. S12a). The compositional characterization of the product has been examined by EDS. As seen in Fig. S12b, the strong peaks for Sn and O elements come from SnO_2 nanocrystals in the bare SnO_2 nanosheets, whereas the additional Cu elemental peak originates from the copper-grid used in the TEM tests. Additionally, the molar ratio of Sn/Fe is determined to be 99.98:0.02 from the EDS spectrum, indicating the complete dissolution of Fe_2O_3 nanocrystals. Moreover, all the diffraction peaks in the XRD pattern of bare SnO_2 nanosheets can be indexed to tetragonal SnO_2 (JCPDS: 41-1445, Fig. S12c), further confirming the entire removal of Fe_2O_3 nanocrystals in 2D SnO_2–Fe_2O_3 nanosheets.

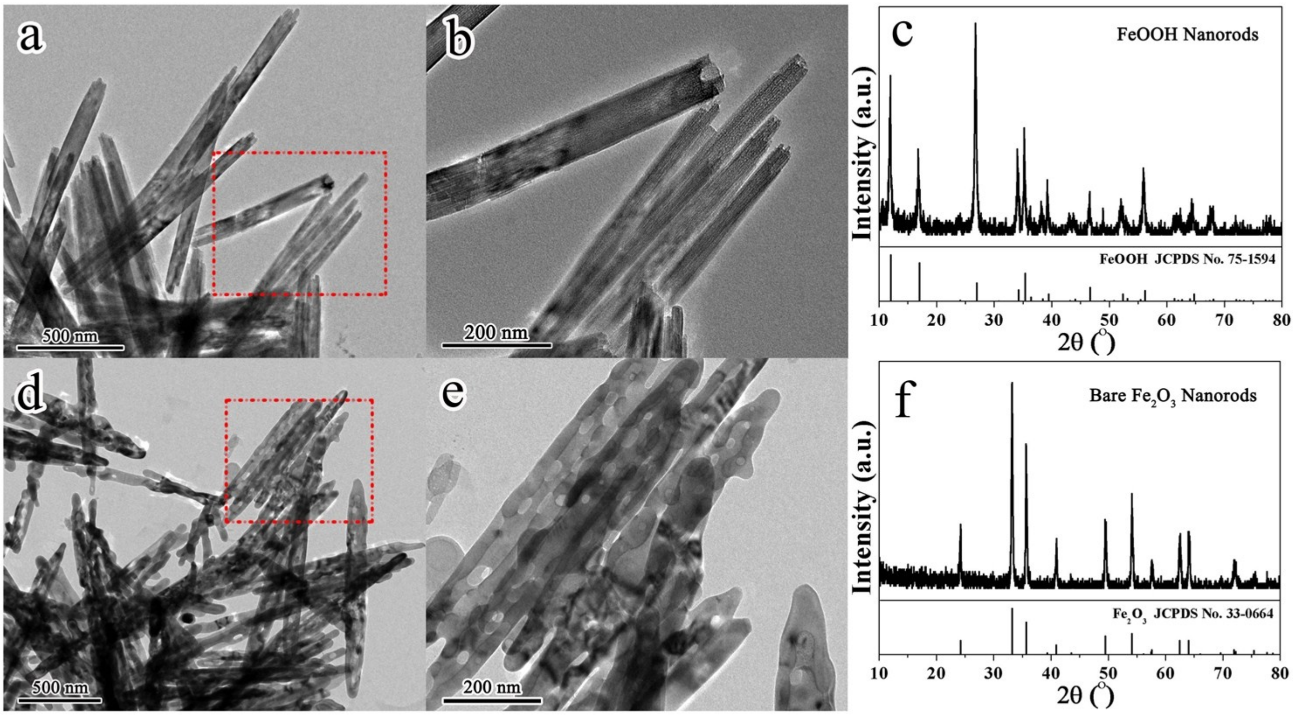

Fig. S13 TEM images (a, b) and XRD pattern (c) of the FeOOH nanorod precursors and TEM images (d, e) and XRD pattern (f) of the bare Fe_2O_3 nanorods.

FeOOH nanorods was prepared by a facile hydrothermal route. Typically, 80 ml of 0.5 M $FeCl_3$ solution was transferred into a 100 mL Teflon-lined stainless steel autoclave and heated at 90 ^oC for 12 h, yielding the FeOOH nanorods (Fig. S13a-c). As observed, the product manifests a typical rod-like morphology (Fig. S13a, b), and the observed crystalline phase can be indexed to tetragonal FeOOH (JCPDS: 75-1594, Fig. S13c), indicating the formation of FeOOH nanorods.

The FeOOH nanorods can serve as precursors for the selective formation of iron oxide nanorods including hematite, magnetite, and maghemite under appropriate conditions. Herein, the FeOOH nanorods was annealed at 600 ^oC in air for 3 h at a heating rate of 1 K min^{-1}. After annealing, the observed crystalline phase has transformed from tetragonal FeOOH to hexagonal Fe_2O_3 (JCPDS: 33-0664, Fig. S13f), indicating the successful transformation from FeOOH precursor to Fe_2O_3 product. The TEM images indicate that the oxide product inherits the 1D rod-like morphology of the FeOOH precursor (Fig. S13d, e). Moreover, the Fe_2O_3 product exists in the form of porous structures with abundant cavities in the nanorods.

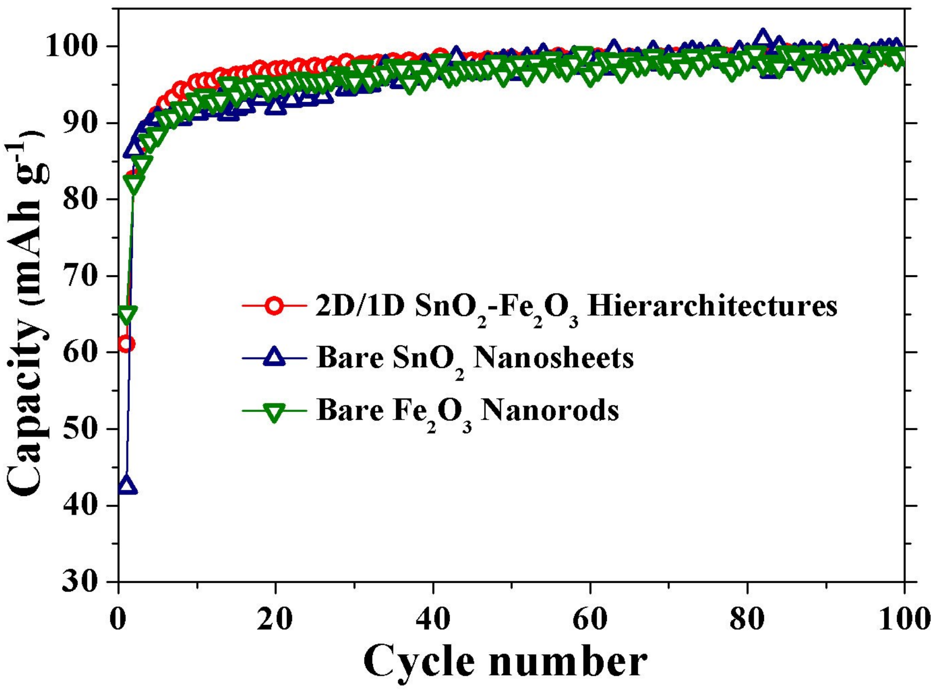

Fig. S14 Coulombic efficiencies versus cycle numbers for the 2D/1D SnO_2–Fe_2O_3 hierarchitectures, bare SnO_2 nanosheets, and bare Fe_2O_3 nanorods.

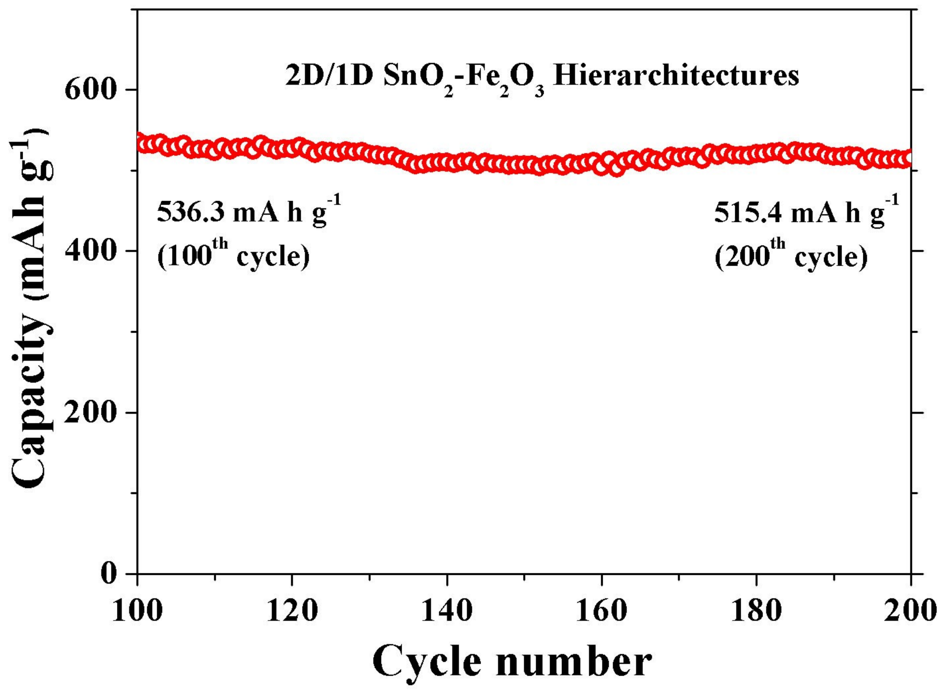

Fig. S15 Discharge capacities versus cycle numbers for the 2D/1D SnO_2–Fe_2O_3 hierarchitectures in the potential range of 0.01-3 V at a current density of 100 mA g^{-1} from 100th to 200th cycles.

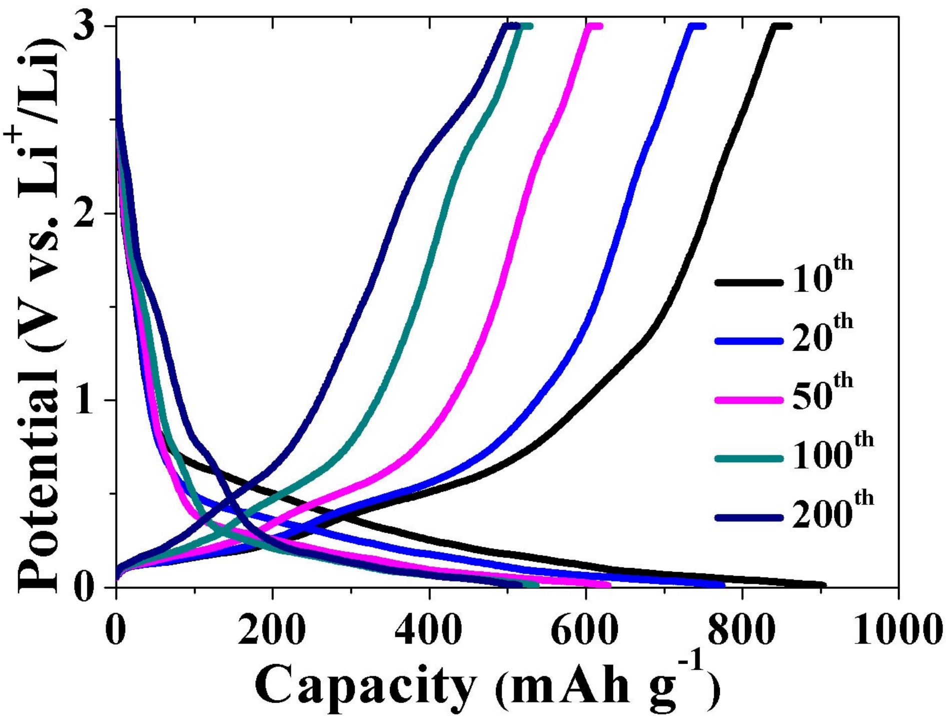

Fig. S16 The 10th, 20th, 50th, 100th and 200th discharge and charge curves for the 2D/1D SnO_2–Fe_2O_3 hierarchitectures.